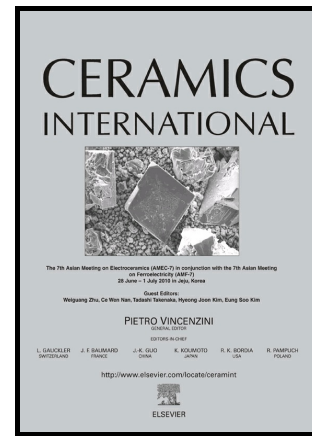


# Author's Accepted Manuscript

Sr-doped forsterite nanopowder: Synthesis and biological properties

R. Gheitanchi, M. Kharaziha, R. Emadi



www.elsevier.com/locate/ceri

PII: S0272-8842(17)31268-3

DOI: <http://dx.doi.org/10.1016/j.ceramint.2017.06.054>

Reference: CER115576

To appear in: *Ceramics International*

Received date: 15 February 2017

Revised date: 7 June 2017

Accepted date: 8 June 2017

Cite this article as: R. Gheitanchi, M. Kharaziha and R. Emadi, Sr-doped forsterite nanopowder: Synthesis and biological properties, *Ceramic International*, <http://dx.doi.org/10.1016/j.ceramint.2017.06.054>

This is a PDF file of an unedited manuscript that has been accepted for publication. As a service to our customers we are providing this early version of the manuscript. The manuscript will undergo copyediting, typesetting, and a review of the resulting galley proof before it is published in its final citable form. Please note that during the production process errors may be discovered which could affect the content, and all legal disclaimers that apply to the journal pertain.

# Sr-doped forsterite nanopowder: Synthesis and biological properties

R. Gheitanchi, M. Kharaziha\* . R. Emadi

Department of Materials Engineering, Isfahan University of Technology, Isfahan 84156-83111, Iran

\*Corresponding author. ma.kharaziha@gmail.com

## Abstract

Nanoscale forsterite ( $\text{Mg}_2\text{SiO}_4$ ) has recently been proposed for bone tissue engineering application. Due to the special role of strontium (Sr) in bone remodeling, the stimulation of bone formation and reduction in bone resorption, the modification of forsterite by doping with Sr is expected to increase bioactivity and biocompatibility. The aim of this study was to incorporate Sr (0, 0.05, 0.1, 0.2 and 0.4 at.%) into forsterite using sol-gel method and to investigate the effect of Sr content on the phase composition, *in vitro* apatite-formation ability as well as osteoblast-like MG63 cell viability. Results demonstrated that while forsterite was the main phase of all Sr-doped forsterite nanopowders,  $\text{Sr}_2\text{MgSi}_2\text{O}_7$ , MgO,  $\text{MgSiO}_3$  were present as the minor phases depending on the Sr content. Moreover, the presence of Sr atom influenced the crystallite and particle size as well as lattice parameters of the forsterite powder, while did not significantly change the morphology of particles. Noticeably, the incorporation of Sr up to 0.2 at.% enhanced the average crystallite size (from 25.3 nm to 45.9 nm) and particle size ( $31.0 \pm 3.9$  nm to  $62.9 \pm 11.8$  nm) of pure forsterite powder. Additionally, according to the Rietveld refinement, the incorporation of Sr up to 0.2 at.% increased the lattice parameters of forsterite more than 0.1%, depending on the Sr content. *In vitro* bioactivity assessment in simulated body fluid (SBF) revealed while all Sr-forsterite samples possessed greater bioactivity than pure forsterite nanopowder, the incorporation of 0.1 at.% Sr revealed improved bioactivity compared to other Sr-forsterite samples. However, according to MTT assay, while all forsterite-based ceramics significantly improved the cell proliferation compared to tissue culture plate (TCP) and forsterite nanopowder, Sr-forsterite nanopowders consisting of 0.05-0.1 at.% Sr revealed a considerably promoted cell proliferation. In conclusion, Sr-forsterite nanopowder could be a promising candidate for bone tissue engineering and reconstruction of bone defects such as osteoporosis.

**Keywords:** Forsterite; Strontium; Rietveld refinement; Bioactivity; Bone tissue engineering.

## 1. Introduction

Nanoscale forsterite ( $\text{Mg}_2\text{SiO}_4$ ) has recently been introduced as a potential bioactive ceramic for bone tissue engineering due to its biocompatibility, osteoconductivity and higher mechanical characteristics compared to other bioactive ceramics such as hydroxyapatite (HA) and bioactive glass [1, 2]. Forsterite consists of Si and Mg ions with the significant role in the human body. While silicon is a fundamental element in skeletal development, magnesium is directly associated with the mineralization of calcined tissues and ultimately influences the mineral metabolism [2-5]. These properties make forsterite suitable for orthopedic, maxillary-facial surgery and dentistry applications as membranes, coatings, and bulk constructs [6-9]. However, the high stability of forsterite chemical structure may support the possible cationic substitution which could be a promising strategy to improve biological performance of the bone substitute materials [10, 11].

Strontium, a naturally occurring trace element in the human body, is available in the inorganic phase of the bone. In fact, 98% of the body strontium content can be found in the skeleton. Specifically, the strontium content in a fresh bone was almost 4- and 2.5-fold superior to that of in the old compact and cancellous bone, respectively. Due to the antiresorptive and anabolic properties, strontium has been introduced as a treatment approach for osteoporosis. Strontium can incorporate into bone via two approaches: (a) surface exchange comprising the inclusion of strontium into the crystal lattice of the bone inorganic component and (b) ionic substitution in which strontium is taken up by ionic exchange with Ca of bone inorganic component [12, 13]. Moreover, strontium plays a critical role in the bone growth consisting of motivating osteoblast differentiation and hindering osteoclast activity. Therefore, the modification of bioceramics by partial or full substitution of strontium with other cationic elements is expected to increase both bioactivity and biocompatibility [14]. In the last decades, the incorporation of strontium in various bioceramics such as calcium phosphate [15, 16], bioactive glass [17, 18], calcium silicate [19, 20] and bone cement [21-23] has gained a great interest. Results revealed that in the case of HA, strontium substitution enhanced its mechanical properties and bioactivity making it suitable for normal functioning inside the body [24]. Moreover, strontium substitution could stabilize the HA crystals against grain growth and phase transformation during sintering at elevated temperatures [25]. In addition, it was demonstrated that strontium-containing bioceramics could encourage *in vitro* osteoblast attachment, proliferation, and mineralization as well as *in vivo* bone growth and

osseointegration [15, 26]. Despite the wide researches on the strontium- containing bioceramics, based on our knowledge, strontium-doped forsterite has never been evaluated.

The aim of this study was incorporation of strontium into forsterite nanopowder (Sr-forsterite) and to investigate the effects of strontium substitution on the structural, chemical and biological properties of forsterite nanopowder. In this regard, due to the limited solubility, forsterite nanopowders with low strontium content ranging from 0.05 at.% to 0.4 at.% were synthesized using sol-gel technique. It is expected that the presence of three human essential ions in Sr-forsterite (Mg, Si and Sr ions) might improve the bioactivity, biodegradation and cell function compared to forsterite nanopowder and other bioactive ceramics such as HA.

## 2. Materials and methods

### 2.1. Synthesize of Sr-forsterite and pure forsterite nanopowders

Strontium substituted forsterite (Sr-forsterite) was designed at different Mg/Si ratios as shown in details in Table 1 while Mg+Sr/Si was set to 2/1. Based on different Sr contents, samples were named as  $Mg_{2-x}Sr_xSiO_4$  in which the compositional parameter 'x' was 0.05, 0.1, 0.2, 0.4 at.%. Forsterite nanopowder was synthesized using a sol-gel method developed by our group, recently [5]. The same process was used to synthesize Sr-forsterite powder with minor modification as schematically illustrated in Fig. 1. Briefly, magnesium nitrate hexahydrate ( $Mg(NO_3)_2 \cdot 6H_2O$ , Merck, 99.99% purity) and strontium nitrate ( $Sr(NO_3)_2$ , Merck, 99.99% purity) were dissolved in 50 ml deionized (DI) water on a magnetic stirrer. After complete dissolution, colloidal silica ( $SiO_2$ , 34 wt.% solid fraction, Sigma) was added and mixed to be homogenized. Subsequently, 83 wt.% sucrose ( $C_{12}H_{22}O_{11}$ , Merck, 99.99% purity) solution and 1.3 wt.% polyvinyl alcohol (PVA, Merck, Mw =72,000 gr/mol) solution were added to above solution. After adjusting the pH value to about 1 using 1 M nitric acid solution, the solution was mixed homogeneously by constant stirring for 2 h at 80 °C. PVA and sucrose were used in the forsterite synthesize procedure due to the dissimilar hydrolysis and condensation rates of silica and alkoxides which results in chemical inhomogeneity of the gels and, hence, undesirable phases in the final product. During the synthesize process, nitric acid could break sucrose into glucose and fructose. Decomposed products consisted of OH and COOH groups which could inspire the binding of  $Mg^{2+}$  ions in the homogeneous solution. In other word, PVA could develop polymeric network which could trap colloidal silica nanoparticles leading to their homogenous distribution[27]. In order to complete hydrolysis processes, aging treatment was carried out at ambient temperature for 2 h. As prepared solutions were then heated on a hot plate at 100 °C for enough time to complete dehydration and change into a voluminous, black and fluffy gel. Finally, as prepared dried gels were calcined in a furnace at different temperatures between 800 and 1000 °C for 2 h.

## 2.2. Characterization of Sr-forsterite powder

The phase composition, lattice parameter as well as crystallite size of synthesized powders (forsterite and Sr-forsterite powders) were determined by means of X-ray diffraction (XRD, Philips XPert) using Ni filtered Cu  $\alpha$  ( $\lambda_{\text{Cu}\alpha} = 0.154$  nm, radiation at 40 kV and 30 mA), which scanned the diffraction angles ( $2\theta$ ) between  $20^\circ$  and  $80^\circ$  with a step size of  $0.05^\circ$  and a count time of 1.25 s per step. To determine phase compositions, the patterns were matched to the Joint Committee on Powder Diffraction Standards (JCPDS) reference files. The crystallite size of the powders was calculated from XRD pattern with standard data compiled by the International Center for Diffraction Data (ICDD) using the modified Scherrer formula (eq. 1)[28]

$$\ln \beta = \ln \frac{k\lambda}{L} + \ln \frac{1}{\cos\theta} \quad (1)$$

where L is the crystallite size (nm),  $\lambda$  is the wavelength of Cu  $\alpha$  radiation ( $\lambda = 1.5404 \text{ \AA}$ ),  $\beta$  is the full width at half maximum (FWHM) for the diffraction peak under consideration (in radian),  $\theta$  is the diffraction angle ( $^\circ$ ) and k is the broadening constant (0.9). For this purpose, some diffraction peaks consisting of (131), (112) and (222) which revealed the benefit of being well-separated and high intensities, were selected for the estimation. It needs to mention that, as the broadening of peaks could be due to two sources of instrumental and sample contributions, to measure the instrumental broadening contribution of the diffractometer ( $\beta_{\text{instrument}}$ ), SiO<sub>2</sub> (quartz) was used as standard. To investigate the effects of strontium content on the crystallographic structure of forsterite, Rietveld refinement was employed to estimate the lattice parameters. For Rietveld refinement studies, the powders were heat-treated at a predetermined temperature of  $1000 \text{ }^\circ\text{C}$ , followed by a dwelling time of 2 h and then cooled to room temperature. The Maud software with the fundamental parameters approach was employed for Rietveld refinements. Rietveld refinement was performed using the structural model of ICSD card number of 9000319 for forsterite. Refined parameters were scale factor, specimen displacement, and background as Chebyshev polynomial of fifth grade and 1/x function, crystallite size, micro-strain, and lattice parameters.

Functional groups of forsterite and Sr-forsterite powders were evaluated by Fourier transform infrared (FTIR). The spectrum was recorded using Bruker Tensor-27 in the  $400\text{--}4000 \text{ cm}^{-1}$  region. The morphology and elemental composition of the synthesized powders were investigated using scanning electron microscopy (SEM Philips XL30:Eindhoven) equipped with energy dispersive spectroscopy (EDS). Moreover, transmission electron microscope (TEM, Philips, 208S 100 KV) was applied to evaluate the morphology and particle size distribution of the synthesized powders. In this regard, the particle size of powders was estimated by Image J software (n=50).

### 2.3. *In vitro* bioactivity evolution of Sr-forsterite powder

*In vitro* bioactivity of forsterite and Sr-forsterite was studied by soaking the samples in simulated body fluid (SBF) solution prepared as described by Bohner *et al.*[29]. The obtained powders were uniaxially pressed at 300 MPa to fabricate pellets with 5 mm in diameter and 10 mm in thickness. As prepared pellets were then soaked in 10 ml SBF (pH 7.4) at 37 °C for 28 days. After soaking, the samples were dried at 100 °C for 1 day. SEM and EDS analysis were used to investigate the formation of apatite on the surface of samples. SBF solutions were collected at the pre-determined intervals to determine the ion concentrations of Ca, Mg, Sr and P ions by inductively coupled plasma atomic emission spectroscopy (ICP) (AES; Varian, USA). In addition, pH values of SBF solutions were recorded using an electrolyte type pH meter (Metrohm, Switzerland 827).

### 2.4. Cell culture

In order to investigate the effect of strontium content on the cytotoxicity of forsterite, MG63 osteoblast-like cell line from the National Cell Bank of Iran at the Pasteur Institute (NCBI code: C555) was cultured on the forsterite and Sr-forsterite pellets and cell proliferation was investigated. MG63 cells were cultured in Dulbecco's Modified Eagle Medium (DMEM-low glucose, Bioidea, Iran) containing 10 vol.% fetal bovine serum (FBS) (Bioidea, Iran) and 1 vol.% streptomycin/ penicillin (Bioidea, Iran) at 37 °C under 5% CO<sub>2</sub> condition. Prior to cell seeding, the samples were washed thrice with PBS and sterilized in 70 (v/v)% ethanol for 30 min followed by 2 h exposure to ultraviolet (UV) light. Finally, the samples were soaked in the complete culture medium overnight prior to cell seeding. After reaching 70-80% confluency, the cells were detached with 0.25 (v/v)% trypsin/EDTA solution (Bioidea, Iran) and counted by trypan blue assay. Finally, they were collected from the flask, counted and seeded on the samples as well as tissue culture plate (TCP) (control) with a density of 10<sup>4</sup> cells/well. MG63 Cells were incubated for 1, 3 and 7 days at 37 °C under 5% CO<sub>2</sub> condition while the medium was aspirated after 3 days interval and fresh medium was added to each well.

#### 2.4.1. Cell viability study

The relative viability of cells was studied by 3-(4,5-dimethylthiazolyl-2)-2,5-diphenyl tetrazolium bromide (MTT, Sigma-Aldrich) colorimetric assay. At the predicted times of culture (1, 3 and 7 days), the medium was discarded, the wells were washed with PBS and the samples were incubated with MTT solution (0.5 mg/ml MTT reagent in PBS) for 4 h. The dark blue formazan crystals were solubilized with dimethyl sulfoxide (DMSO, Sigma) as the MTT solvent and kept for 30 min at 37 °C. Subsequently, 100 µL of dissolved formazan solution of each

sample was moved to a 96-well plate and the optical density (OD) of each well was measured with a microplate reader (Bio Rad, Model 680 Instruments) against DMSO (blank) at a wavelength of 540 nm and a reference filter of 630 nm. The relative cell survival was calculated based on the following equation (eq. 2):

$$\text{Relative cell survival (\%)} = \frac{A_{\text{sample}} - A_{\text{b}}}{A_{\text{control}} - A_{\text{b}}} \quad (2)$$

where  $A_{\text{sample}}$ ,  $A_{\text{b}}$  and  $A_{\text{control}}$  are the absorbance of sample, blank (DMSO) and control (TCP), respectively.

### 2.5. Statistical analysis

The data of MTT assay was evaluated using one-way ANOVA analyses using GraphPad Prism Software (V.6) and reported as mean  $\pm$  standard deviation (SD).  $P$ -value  $<0.05$  was applied to be significant.

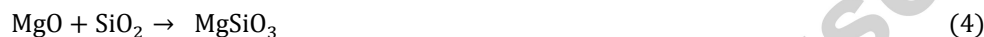
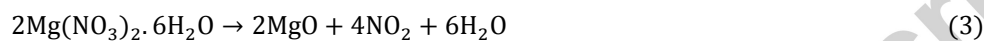
## 3. Results and discussion

### 3.1. Characterization of Sr-forsterite powder

In order to evaluate the effect of calcification temperature on the chemical composition of forsterite, F2 powder ( $\text{Mg}_{1.9}\text{Sr}_{0.1}\text{SiO}_4$ ) was calcined at various temperatures (800, 900 and 1000 °C) (Fig. 2(a)). Results demonstrated the effective role of temperature to control the calcification process. At 800 °C, in addition to forsterite as the major phase, the secondary phases could be detected consisting of enstatite ( $\text{MgSiO}_3$ ) and magnesium oxide (MgO). By increasing the calcification temperature upon 1000 °C, the intensity of three main characteristic peaks of forsterite assigned for (112) (at  $2\theta=36.536$ ), (131) (at  $2\theta=35.730$ ), and (222) (at  $2\theta=52.274$ ) crystallographic planes enhanced while the secondary phases reduced which might be due to the role of temperature to accelerate the incorporation of strontium into forsterite structure. Moreover, according to modified Scherer formula, the crystallite size of forsterite powder enhanced from  $39.7\pm 2$  nm to  $45.5\pm 1$  nm with increasing calcination temperature from 800 °C to 1000 °C. A similar result was reported by Mardziah *et al.* [25], who incorporated Sr within HA at different temperatures and showed that the crystallinity of HA enhanced with increasing the calcination temperatures from 500 °C to 900 °C. Moreover, they pointed out the enlargement of crystallite size of the powder from 10 nm to 50 nm. Based on the effective role of temperature on the chemical reactions during the calcification, 1000 °C was selected to calcify other samples consisting of various amounts of strontium content.

- 1) XRD patterns of the forsterite and Sr-forsterite powders containing various amounts of strontium components (0, 0.05, 0.1, 0.2 and 0.4 at.%) calcified at 1000 °C are presented in Fig. 2(b). According to the

modified Scherer's equation (eq. 1) and Rietveld refinement, the crystallite size (nm), phase composition (wt.%) and lattice parameters of a, b and c were estimated (Table 2). The agreement indices such as Sig (GoF),  $R_{wp}$  and  $\chi^2$ , of the Rietveld refinements were presented in Table S1. In the absence of strontium (F0), only forsterite characteristic peaks could be detected without any impurity and secondary phase. After the incorporation of strontium, while forsterite was detected in all samples, the second or third phases could be detected, depending on the strontium content. For instance, the incorporation of 0.4 at.% strontium ( $Mg_{1.9}Sr_{0.1}SiO_4$ ) resulted in the formation of enstatite ( $MgSiO_3$ ), magnesia (MgO) and  $Sr_2MgSi_2O_7$ . The synthesise of forsterite is based on the reaction between MgO and  $SiO_2$  according to the following equations from the magnesium nitrate hexahydrate (eqs. 3, 4 and 5):



According to above equations, magnesia (MgO) and enstatite ( $MgSiO_3$ ) were the intermediate components formed during the calcification of forsterite. In the presence of low amount of strontium nitrate and according to the ratio of (Mg+Sr)/Si=2/1, magnesium replaced with strontium ions during the synthesizing of forsterite powder. However, according to the XRD patterns of F1 and F2, the intermediate phases of magnesia and enstatite were remained after calcification at 1000 °C confirming the inhibitory role of Sr in the forsterite formation. Substitution of magnesium with strontium ions was confirmed via the calculation of lattice parameters of forsterite (Table 2). The main peak of forsterite located at  $2\theta=36.652^\circ$  corresponding to (112) plane shifted to low angles ( $2\theta=36.535$  and  $36.536$  at F1 and F2, respectively) (Fig. 2(c)). Moreover, the corresponding peaks of (131) and (222) planes at F1 and F2 samples were appeared at  $2\theta=35.751$ ,  $2\theta=52.266$  and  $2\theta=35.730$  and  $2\theta=52.274$ , respectively. Compared to the consequent peaks of (131) and (222) of forsterite ( $2\theta=35.863$  and  $2\theta=52.375$ , respectively), these peaks shifted to smaller degrees which could be due to the bigger size of Sr atoms than Mg (ionic radius of 1.12 °A versus 0.72 °A) leading to an increase in a, b and c lattice parameters (Table 2). Noticeably, a, b and c lattice parameters were enhanced around 0.11%, 0.098% and 0.13%, respectively when Sr content enhanced to 0.2 at.% ( $Mg_{1.8}Sr_{0.2}SiO_4$ ). In the presence of high amounts of Sr content (> 0.2 at.%), Sr could not substitute Mg ions resulted in the formation of new phase during the calcification, according to the following equations (eqs. 6 and 7):



Therefore, magnesia, formed as the intermediate phase during forsterite formation, could chemically interact with strontium oxide synthesized by the decomposition of strontium nitrate and silica (eq. 6). Hence,  $\text{Sr}_2\text{MgSi}_2\text{O}_7$  was synthesized instead of enstatite as the final secondary phase along with forsterite. At this condition, the main peak of forsterite at  $2\theta=36.652^\circ$  corresponded to (112) plane was shifted to  $2\theta=36.477^\circ$ . However, more increasing Sr content up to 0.4 at.% (F4) did not change the lattice parameters which might be due to the partial substitution of strontium ions as well as the formation of the secondary phase of  $\text{Sr}_2\text{MgSi}_2\text{O}_7$ . Hesaraki *et al.* [10] also similarly reported an increase in the lattice parameters of beta tricalcium phosphate unit cell after substitution of Sr ions. They revealed that, while both a and c parameters enhanced with the incorporation of ~7 mol% of Sr (Ca/Sr:2.8/0.2) to  $\beta$ -TCP, lattice parameters remained approximately constant due to the partial replacement of Sr ions with calcium. They also revealed that the replacement of strontium ions within  $\beta$ -TCP more than ~7 mol% resulted in the formation of secondary phases like strontium phosphate. Moreover, according to Table 2, the crystallite size of forsterite powder enhanced with increasing Sr substitution up to 0.2 at.% from 25.3 nm (at F0) to 45.8 nm (at F3), which could be attributed to crystal growth due to lattice strain by larger Sr ions (1.12 Å) in the forsterite lattice. Moreover, the lattice parameters (a, b and c) of forsterite increased with the addition of Sr up to 0.2 at.%, whereas the crystallite size and lattice parameters remained approximately constant by adding more Sr (0.4 at.%) ( $\text{Mg}_{1.6}\text{Sr}_{0.4}\text{SiO}_4$ ) which might be due to the formation of secondary phases like  $\text{Sr}_2\text{MgSi}_2\text{O}_7$ . Due to the high impurity of sample F4, further experiments were conducted to three other samples (F1, F2 and F3).

The FT-IR spectra of pure forsterite nanopowder (F0) and Sr-forsterite consisting of different Sr contents (F1, F2 and F3) (Fig. 3) confirmed the incorporation of strontium within forsterite structure. The FTIR spectra of forsterite consisted of the characteristic peaks of  $\text{SiO}_4$  stretching and  $\text{SiO}_4$  bending in the range of 830–1007  $\text{cm}^{-1}$  and 500–620  $\text{cm}^{-1}$ , respectively. Moreover, the presence of the peak around 420  $\text{cm}^{-1}$  attributed to Mg-O bonds of the  $\text{MgO}_6$  octahedral confirmed the formation of forsterite. A similar result was observed in other works [5, 30]. Moreover, the absorption bands around 3477  $\text{cm}^{-1}$  and 1619  $\text{cm}^{-1}$  were related to the hydroxyl (OH) group indicating the absorbed water. In addition to the typical bands of forsterite, FTIR spectra of Sr-forsterite consisted of the absorption band at 1465  $\text{cm}^{-1}$  attributed to the asymmetric stretching of C–O bonds suggesting the incorporation

of carbonates into the forsterite lattice during preparation [31]. This result was in agreement with the work of Kanno *et al.* [32] who found that Sr-substituted HA can accommodate more carbonate ions into its structure. Moreover, the substitution of strontium ions resulted in shifting the characteristic peaks of forsterite. For instance, the characteristic peaks of  $\text{MgO}_6$  and the stretching and bending mode of  $\text{SiO}_4$  appeared at  $419\text{ cm}^{-1}$ ,  $827\text{-}1006\text{ cm}^{-1}$  and  $499\text{-}617\text{ cm}^{-1}$ , respectively at F2 samples attributing the increase in the average dimensions of the cations [11].

The morphology of forsterite and Sr-forsterite (0, 0.05, 0.1 and 0.2 at.% strontium) powders was investigated by SEM and the images are depicted in Fig. 4. Moreover, the average particle sizes of the synthesized samples estimated using Image J software were presented in Table 2. Results revealed that Sr substitution did not change the morphology of forsterite powder. However, inconsistent with the crystallite size extracted from XRD analysis, the average particle sizes of the powders extracted from SEM images significantly enhanced from  $31.0 \pm 3.6$  (at F0) to  $62.9 \pm 11.8$  (at F3). EDS analysis employed to investigate the elemental composition of forsterite and Sr-forsterite nanopowders (Fig. 4) also confirmed the presence of magnesium (Mg), oxygen (O), silicon (Si) and strontium (Sr) in the structure of the synthesized Sr-forsterite nanopowders. However, the magnesium content decreased while strontium component increased confirming the substitution of magnesium with strontium, with increasing the amount of strontium concentration from 0 (F0) to 0.2 at.% (F3),

TEM micrographs of the forsterite (F0) as well as  $\text{Mg}_{1.9}\text{Sr}_{0.1}\text{SiO}_4$  (F2) nanopowders (Fig. 5(a) and (c)) confirmed that while both powders consisted of spherical-like particles with uniform size, the average particles size enhanced with the introduction of Sr in the forsterite. According to the particle size histograms (Fig. 5(b) and (d)), the distribution of particle size in F0 sample was in the range of 20-50 nm which enhanced to 80-160 nm at F2 sample. Our result was in agreement with the results of other researchers who incorporated Sr in HA [33]. For instance, Qaisar *et al.* [34] investigated the effects of Sr on the particles size of HA nanopowder and showed that Sr substitution led to enlarged particles thought to be due to the increase in ionic radius from calcium to strontium.

### 3.2. *In vitro* apatite forming ability in SBF

The apatite formation ability of compacted forsterite and Sr-forsterite was evaluated using soaking the samples in SBF solution for 30 days at  $37 \pm 0.5\text{ }^\circ\text{C}$ . Fig. 6 represents the SEM images and EDS spectra using area microanalysis of samples after soaking in SBF solution for 28 days. Cauliflower-like particles were deposited on the surface of samples and covered it completely. This morphology was similarly observed in the previous researches

and was attributed to the bone like apatite deposited from SBF solution [5, 35]. EDS spectra of the samples after 28 days soaking in SBF solution confirmed that these precipitations consisted of calcium and phosphorus with various ratios depending on the Sr content in the powders. According to the EDS results, the Ca/P ratios of the cauliflower-like particles deposited on the samples containing 0, 0.05, 0.1 and 0.2 at.% Sr were estimated to be ~1.6, 1.04, 1.53 and 1.33, respectively. Ca/P atomic ratio of depositions was different with that of HA (1.67), specifically at Sr-forsterite powders. It might be due to the substitution of calcium with magnesium and strontium atoms which dissolved during the immersing the samples in SBF solution followed by precipitation during the calcium phosphate formation. Moreover, according to the SEM images, the density of calcium phosphate depositions varied depending on the Sr- content of samples. According to the SEM images, F1 ( $\text{Mg}_{1.9}\text{Sr}_{0.1}\text{SiO}_4$ ) sample revealed the highest density between the samples confirming its greater bioactivity. Gopi *et al.* [35] also showed the bioactivity of pure HA was improved by substitution strontium into it.

The changes of pH value of SBF solution during 28 days soaking of forsterite and Sr-forsterite powders were indicated in Fig. 7(a). The pH value of SBF solutions increased in the first 7 days of soaking, and then gradually decreased at a slow rate towards the end of the soaking period. During soaking the forsterite and Sr-forsterite nanopowders in SBF solution, exchange of  $\text{Mg}^{2+}$  with  $\text{H}^+$  or  $\text{H}_3\text{O}^+$  from SBF solution and formation of silanol bonds (Si-OH) in the initial soaking times led to the increases concentration of  $\text{OH}^-$  and, hence, pH value. Following the migration of calcium, phosphate and hydroxyl ions to the surface of samples and nucleation of bone-like apatite, pH of solution slowly reduced demonstrating the consumption of hydroxyl ions during the formation of apatite layer. The increasing rate of pH and its values depended on the amount of strontium content. Compared to pure forsterite, the soaking of Sr-forsterite nanopowders consisting of 0.5 at.% (F1) and 0.1 at.% (F2) strontium did not significantly enhance the pH values which might be due to the bigger size of strontium atom than magnesium one preventing from rapid release in SBF solution. However, the formation of secondary phases at F2 sample might enhance the defects within the constructs leading to enhanced diffusion of SBF within the samples followed by increasing the ion releasing. Therefore, the pH value of SBF solution was again enhanced during the soaking F2 sample.

Fig. 7(b) indicates the concentration of various ions (Mg, Sr, Ca and P) in SBF solution after 28 days of soaking. Due to the precipitation of bone-like apatite on the samples, the concentration of phosphorous and calcium ions reduced compared to those of SBF solution (the concentration of calcium and phosphorous were 2.5 mM and 1

mM, respectively). However, while the concentration of calcium and phosphorous of SBF solution during the soaking of the Sr-forsterite nanopowder was nearly in the similar range, they were less than those of SBF solution after soaking of forsterite nanopowder confirming the enhanced bioactivity of samples with the substitution of strontium. For instance, while the concentration of calcium and phosphorous ions of SBF solution during the soaking of forsterite nanopowder were about 2.3 and 0.79 mM, respectively, they were reduced to 2.1 and 0.63 mM, respectively, when F2 sample was soaked in SBF solution. In contrast to Ca and P ions, the concentration of Mg and Sr enhanced with increasing Sr-content which could be due to diffusion of these ions during soaking the samples confirming the apatite formation ability.

### 3.3. Cell proliferation study

The proliferation of MG63 cells on the forsterite and Sr-forsterite samples with different concentrations of Sr (0.05, 0.1 and 0.2 at.%) was determined by MTT assay (Fig. 8). The proliferation of MG63 cells cultured on all samples gradually enhanced from day 1 to day 7. Specifically, the proliferation of cells cultured on the 0.05 at.% forsterite nanopowder statistically enhanced from  $77.3 \pm 6.2$  (%control) (at day1) to  $123.6 \pm 8.1$  (% control) (at day 7) ( $P < 0.05$ ). Moreover, after 7 days of culture, compared to pure forsterite nanopowder (F0), Sr-forsterite noticeably enhanced the proliferation of MG63 cells. These results were similarly reported in the previous studies on other Sr-doped ceramics [14, 36-38]. For instance, Gentleman *et al.* [36] synthesized a bioactive glasses (BG) nanopowders ( $\text{SiO}_2\text{-P}_2\text{O}_5\text{-Na}_2\text{O-CaO}$ ) in which 0–100% of the calcium ions were substituted by Sr and investigated their effects on osteoblast and osteoclast behavior. They showed that MTT activity in cells treated with Sr-substituted BG was significantly enhanced compared to non-Sr-containing groups. They suggested that dissolution ions released from the Sr-substituted BG further enhance metabolic activity of cells beyond that caused by the presence of dissolution ions from standard BG.

## 4. Conclusion

In this study, Sr substituted forsterite (Sr-forsterite) with various Sr contents (0, 0.05, 0.1, 0.2 and 0.4 at.%) were successfully synthesized by sol-gel method. Moreover, the effects of Sr concentration on the structural, chemical and biological properties of forsterite nanopowder were investigated. Results confirmed the formation of Sr-forsterite nanopowder with the particle size of 40-62 nm depending on the Sr content. While Sr doping did not change the morphology of forsterite particles, it could enhance the particle and crystallite size of powders. Moreover, in addition to forsterite phase, other phases such as MgO,  $\text{MgSiO}_3$  and  $\text{Sr}_2\text{MgSi}_2\text{O}_7$  were found in the Sr-

forsterite powder, depending on strontium content. Rietveld refinement technique also proved the substitution of  $\text{Sr}^{2+}$  in the forsterite structure due to the bigger lattice parameters of Sr-forsterite compared to those of forsterite. *In vitro* bioactivity evaluation demonstrated that compared to pure forsterite, Sr-forsterite nanopowder revealed improved bioactivity. Furthermore, Sr-forsterite significantly promoted MG63 proliferation compared to forsterite, which might be due to the effective role of strontium to improve cell culture. These results suggest that Sr doped forsterite is an excellent potential candidate for bone tissue engineering applications.

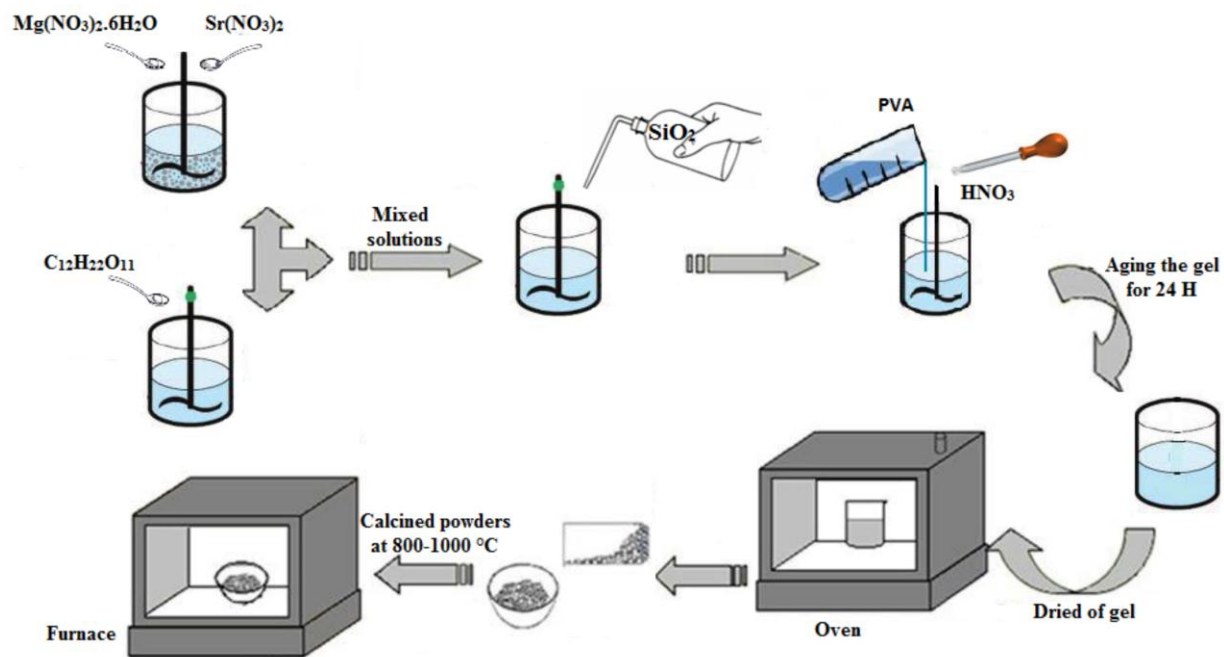
### Reference

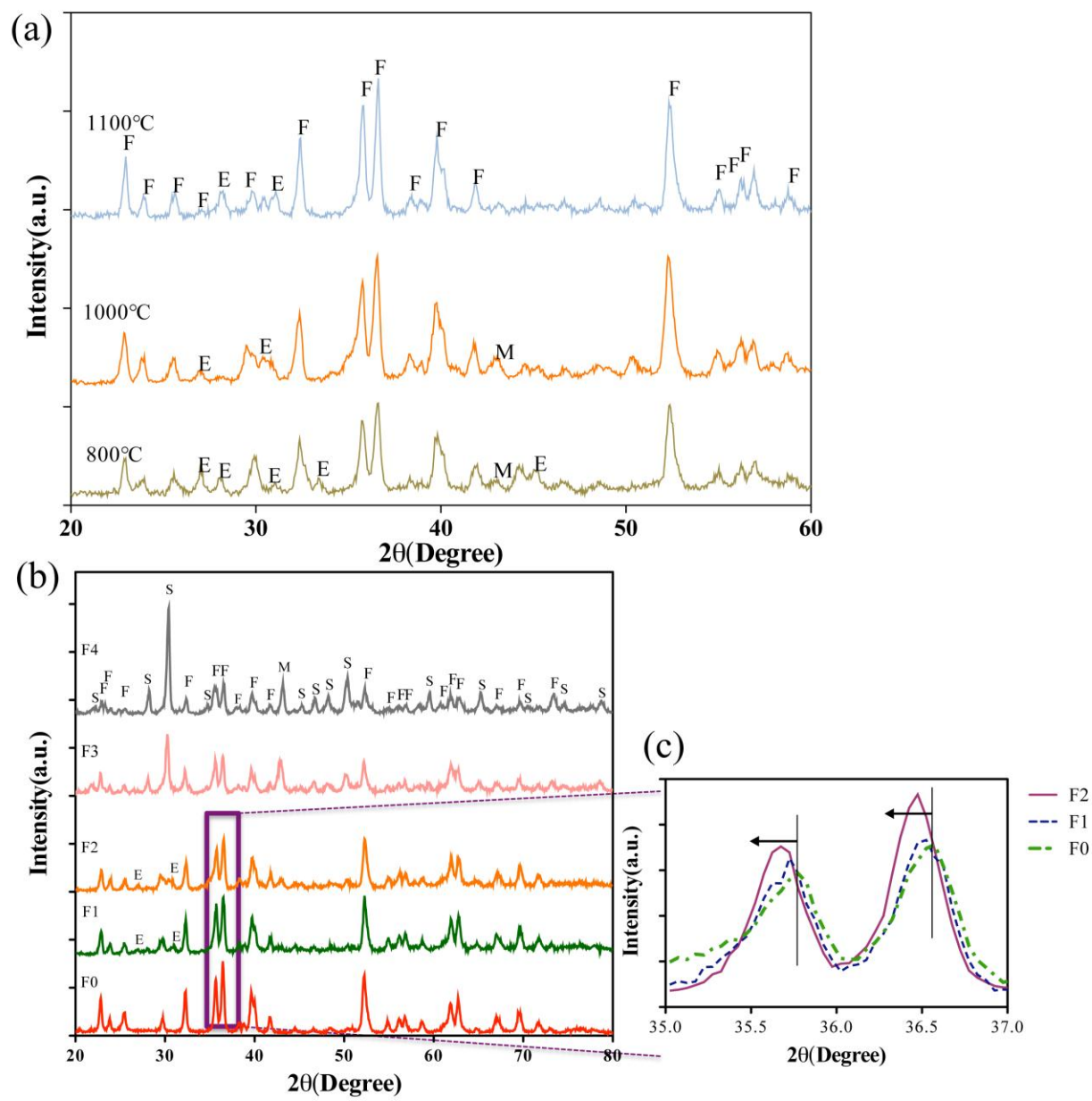
1. Fathi, M.H. and M. Kharaziha, *Two-step sintering of dense, nanostructural forsterite*. Materials Letters, 2009. **63**: p. 1455-1458.
2. Kharaziha, M. and M.H. Fathi, *Improvement of mechanical properties and biocompatibility of forsterite bioceramic addressed to bone tissue engineering materials*. The Mechanical Behavior Of Biomedical Materials, 2010. **3**: p. 530-537.
3. Ni, S., L. Chou, and J. Chang, *Preparation and characterization of forsterite (Mg<sub>2</sub>SiO<sub>4</sub>) bioceramics*. Ceramics International, 2007. **33**: p. 83-88.
4. Kheirkhah, M., et al., *Surface modification of stainless steel implants using nanostructured forsterite (Mg<sub>2</sub>SiO<sub>4</sub>) coating for biomaterial applications*. Surface & Coatings Technology, 2015. **276**: p. 580-586.
5. Kharaziha, M. and M. Fathi, *Synthesis and characterization of bioactive forsterite nanopowder*. Ceramics International, 2009. **35**(6): p. 2449-2454.
6. Fathi, M. and M. Kharaziha, *Mechanochemical synthesis and characterization of nanostructure forsterite bioceramics*. International Journal Of Modern Physics B, 2008. **22**(18n19): p. 3082-3091.
7. Forghani, A., et al., *Novel Fluorapatite-Forsterite Nanocomposite Powder for Oral Bone Defects*. International Journal of Applied Ceramic Technology, 2013. **10**(s1).
8. Kharaziha, M., et al., *PCL-forsterite nanocomposite fibrous membranes for controlled release of dexamethasone*. Journal of Materials Science: Materials in Medicine, 2015. **26**(1): p. 1-11.
9. Jokar, M., et al., *Corrosion and bioactivity evaluation of nanocomposite PCL-forsterite coating applied on 316L stainless steel*. Surface and Coatings Technology, 2016. **307**: p. 324-331.
10. Hesaraki, S., et al., *Phase evaluation and lattice parameters of strontium/magnesium incorporated beta-tricalcium phosphate bioceramics*. Journal of the Australian Ceramic Society, 2012. **48**(2): p. 166-172.
11. Paennarin, H. and S.L. Seet, *Sol-Gel Synthesis and Characterization of Strontium/Zinc-substituted Hydroxyapatites*. CHIANG MAI JOURNAL OF SCIENCE, 2013. **40**(6): p. 1055-1060.
12. Zreiqat, H., et al., *The incorporation of strontium and zinc into a calcium–silicon ceramic for bone tissue engineering*. Biomaterials, 2010. **31**: p. 3175–3184.
13. Curtis, R., et al., *Fixation principles in metaphyseal bone—a patent based review*. Osteoporosis International, 2005. **16**: p. S54-S64.
14. Zhang, W., et al., *Effects of strontium in modified biomaterials*. Acta Biomaterialia, 2011. **7**(2): p. 800-808.

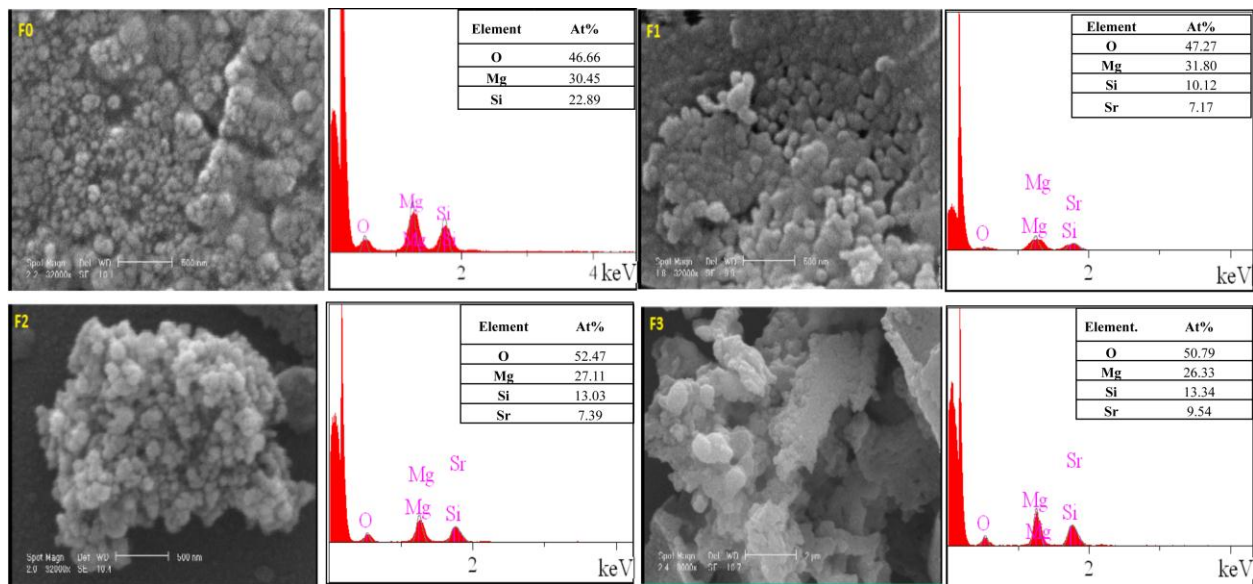
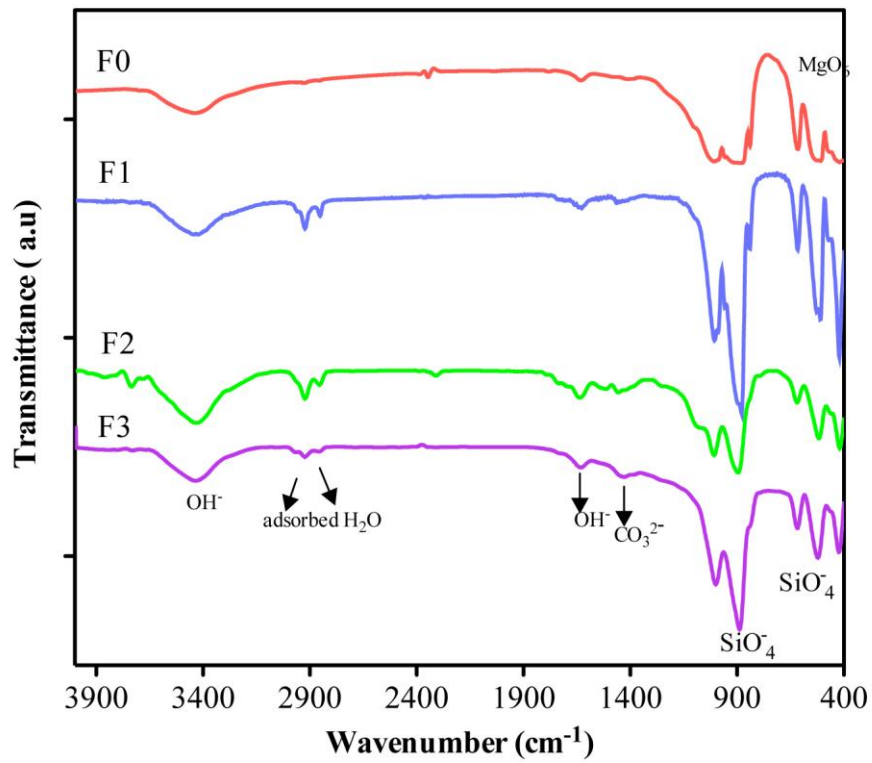
15. Banerjee, S.S., S. Tarafder, and N.M. Davies, *Understanding the influence of MgO and SrO binary doping on the mechanical and biological properties of b-TCP ceramics*. Acta Biomaterialia, 2010. **6**: p. 4167–4174.
16. Kannan, S., F. Goetz-Neunhoeffler, and J. Neubauer, *Synthesis and structural characterization of strontium - and magnesium-co-substituted b-tricalcium phosphate*. Acta Biomaterialia, 2010. **6**: p. 571–576.
17. Strobel, L.A., N. Hild, and D. Mohn, *Novel strontium-doped bioactive glass nanoparticles enhance proliferation and osteogenic differentiation of human bone marrow stromal cells*. Nanopart Res, 2013. **2**: p. 1780-1785.
18. Isaac, J., J. Nohra, and J. Lao, *Effects of strontium-doped bioactive glass on the differentiation of cultured osteogenic cells*. European Cells and Materials, 2011. **21**: p. 130-143.
19. Wu, C., et al., *The effect of strontium incorporation into CaSiO<sub>3</sub> ceramics on their physical and biological properties*. Biomaterials, 2007. **28**: p. 3171-3181.
20. Lin, K., L. Xia, and H. Li, *Enhanced osteoporotic bone regeneration by strontium-substituted calcium silicate bioactive ceramics*. Biomaterials, 2013. **34**: p. 10028-10042.
21. Schumacher, M., et al., *A novel strontium(II)-modified calcium phosphate bone cement stimulates human-bone-marrow-derived mesenchymal stem cell proliferation and osteogenic differentiation in vitro*. Acta Biomaterialia, 2013. **9**: p. 9547–9557.
22. Schumacher, M., et al., *A novel and easy-to-prepare strontium(II) modified calcium phosphate bone cement with enhanced mechanical properties*. Acta Biomaterialia, 2013. **9**: p. 7536–7544.
23. CT, W., et al., *In vivo cancellous bone remodeling on a strontium-containing hydroxyapatite (sr-HA) bioactive cement*. Biomedical Materials Research Part A, 2004. **68**: p. 513-521.
24. Kavitha, M., et al., *Solution combustion synthesis and characterization of strontium substituted hydroxyapatite nanocrystals*. Powder Technology, 2014. **253**: p. 129-137.
25. Mardziah, C., I. Sopyan, and S. Ramesh, *Strontium-doped hydroxyapatite nanopowder via sol-gel method: effect of strontium concentration and calcination temperature on phase behavior*. Artif. Organs, 2009. **23**(2): p. 105-113.
26. Paennarin, H. and L.S. Suphasinee, *Sol-Gel Synthesis and Characterization of Strontium/ Zinc-substituted Hydroxyapatites*. Chiang Mai J. Sci, 2013. **40**: p. 1055-1060.
27. Torkaman, R., et al., *Electrochemical and in vitro bioactivity of nanocomposite gelatin-forsterite coatings on AISI 316 L stainless steel*. Progress in Organic Coatings, 2017. **103**: p. 40-47.
28. Monshi, A., M.R. Foroughi, and M.R. Monshi, *Modified Scherrer Equation to Estimate More Accurately Nano-Crystallite Size Using XRD*. Nano Science and Engineering, 2012. **2**: p. 154-160.
29. Bohner, M. and J. Lemaitre, *Can bioactivity be tested in vitro with SBF solution?* Biomaterials, 2009. **30**: p. 2175-2179.
30. Fathi, M. and M. Kharaziha, *The effect of fluorine ion on fabrication of nanostructure forsterite during mechanochemical synthesis*. Journal of Alloys and Compounds, 2009. **472**(1): p. 540-545.
31. He, L., G. Dong, and C. Deng, *Effects of strontium substitution on the phase transformation and crystal structure of calcium phosphate derived by chemical precipitation*. Ceramics International, 2016.
32. KANNO, T., J.-I. HORIUCHI, and M. KOBAYASHI, *Characteristics of the carbonate ions incorporated into calcium-, partially-strontium-substituted and strontium apatites*. MATERIALS SCIENCE LETTERS, 1999. **18**: p. 1343 – 1345.
33. Krishnan, V., A. Bhatia, and H. Varma, *Development, characterization and comparison of two strontium doped nano hydroxyapatite molecules for enamel repair/regeneration*. Dental Materials, 2016. **32**(5): p. 646-659.
34. Qaisar, S., et al. *Sol-gel synthesis and TEM-EDX characterisation of hydroxyapatite nanoscale powders modified by Mg, Sr or Ti*. in *Journal of Physics: Conference Series*. 2010. IOP Publishing.

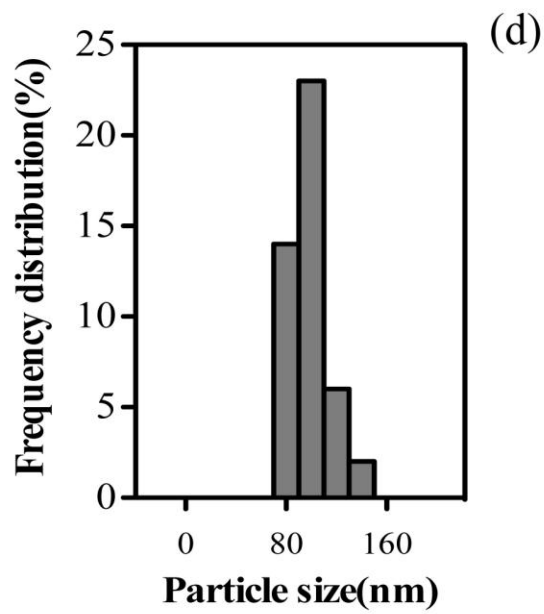
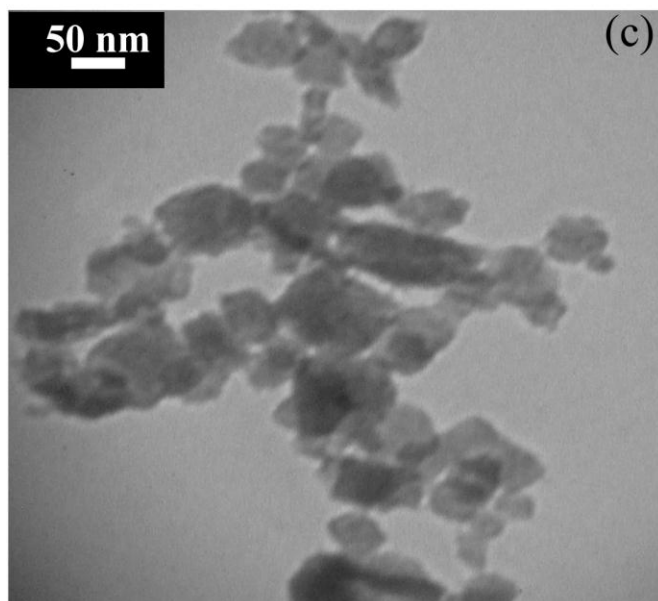
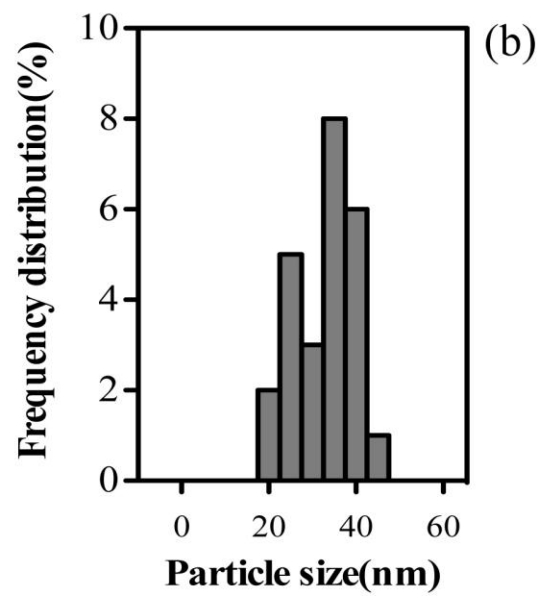
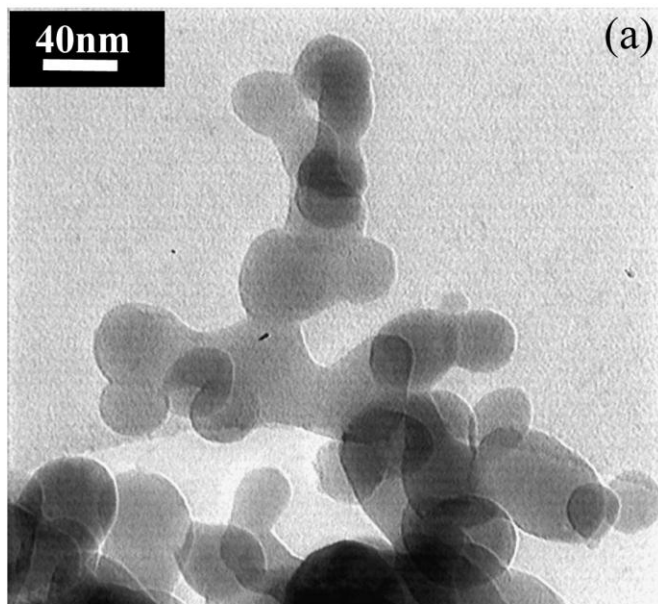
35. Gopi, D., et al., *Strontium, cerium co-substituted hydroxyapatite nanoparticles: synthesis, characterization, antibacterial activity towards prokaryotic strains and in vitro studies*. Colloids and Surfaces A: Physicochemical and Engineering Aspects, 2014. **451**: p. 172-180.
36. Qiu, K., et al., *Effect of strontium ions on the growth of ROS17/2.8 cells on porous calcium polyphosphate scaffolds*. Biomaterials, 2006. **27**(8): p. 1277-1286.
37. Gentleman, E., et al., *The effects of strontium-substituted bioactive glasses on osteoblasts and osteoclasts in vitro*. Biomaterials, 2010. **31**(14): p. 3949-3956.
38. Wu, C., et al., *Strontium-containing mesoporous bioactive glass scaffolds with improved osteogenic/cementogenic differentiation of periodontal ligament cells for periodontal tissue engineering*. Acta biomaterialia, 2012. **8**(10): p. 3805-3815.

Accepted manuscript









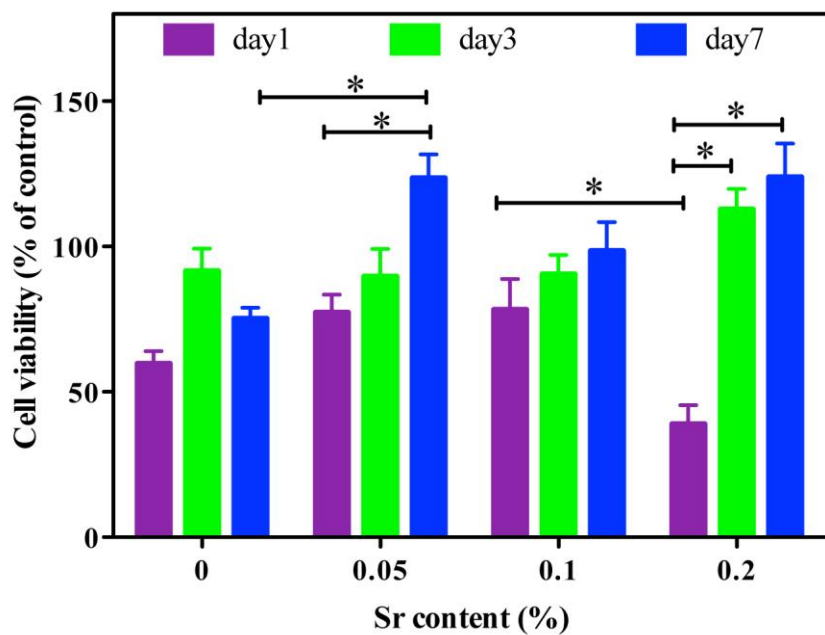
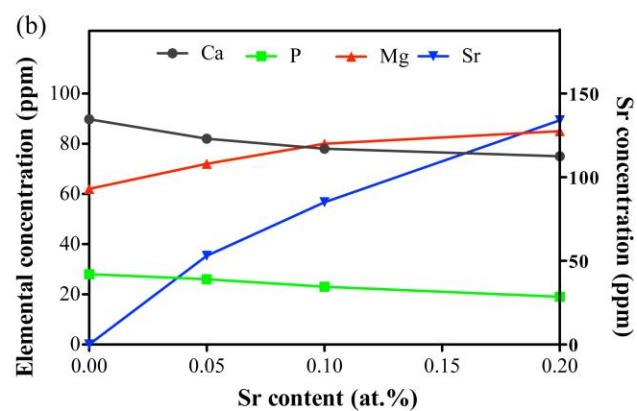
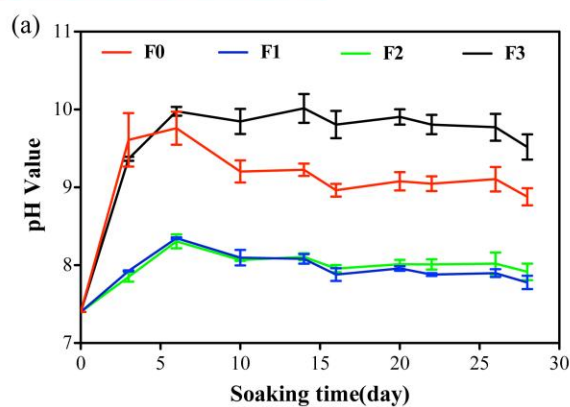
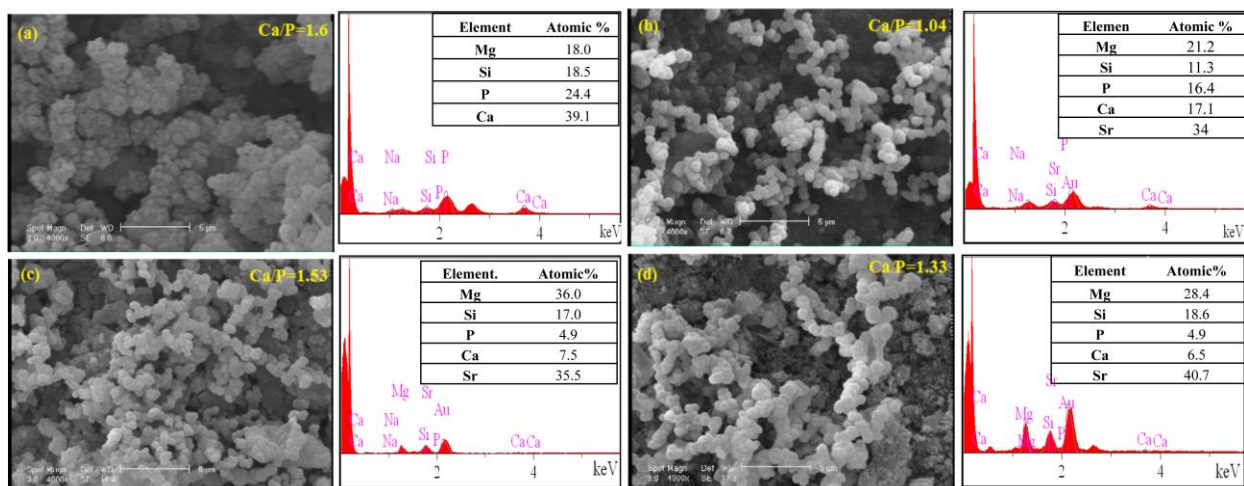


Fig. 1. The schematic representation of the steps involved in Sr-forsterite nanopowder synthesis process.

Fig. 2. Chemical properties of Sr-forsterite powder: a) XRD patterns of  $\text{Mg}_{1.9}\text{Sr}_{0.1}\text{SiO}_4$  powder at different calcification temperatures. b) XRD patterns of forsterite (F0) and Sr-forsterite powders containing various amounts of strontium (0.05 at.% (F1), 0.1 at.%(F2), 0.2 at.% (F3) and 0.4 at.%(F4)) calcified at 1000 ° C. F: Forsterite, M: MgO, S:  $\text{Mg}_{1.9}\text{Sr}_{0.1}\text{SiO}_4$  and E:  $\text{MgSiO}_3$ . c) XRD patterns of F0, F1 and F2 at  $2\theta$  range of 35-37 °

Fig 3. Chemical properties of Sr-forsterite powder: FT-IR spectra of forsterite and Sr-forsterite powders consisting of various amounts of strontium content.

Fig. 4. Structural and chemical properties of Sr-forsterite: SEM micrographs and EDS microanalysis of forsterite and Sr-forsterite powders containing various amounts of strontium (0.05 at.% (F1), 0.1 at.%(F2), 0.2 at.% (F3) and 0.4 at.%(F4)).

Fig. 5. Structural properties of forsterite and Sr-forsterite: TEM micrographs (a and c) and the frequency histogram of particle sizes (b and d) of forsterite (a and b) and  $\text{Mg}_{1.9}\text{Sr}_{0.1}\text{SiO}_4$  (F2) powders.

Fig. 6. *In vitro* bioactivity evaluation of forsterite and Sr-forsterite: SEM micrographs and EDS microanalysis of the forsterite and Sr-forsterite samples after soaking in SBF for 28 days.

Fig 7. *In vitro* bioactivity evaluation of forsterite and Sr-forsterite: a) pH value of SBF solution during the immersion of samples as a function of soaking time and b) the concentration profiles of Ca, P, Mg and Sr ions of SBF solution as functions of strontium content.

Fig. 8. Viability of MG63 cells cultured on various samples using MTT assays after 1, 3 and 7 days of culture. The absorbance was normalized against the control (TCP) at each time interval. (\* $P < 0.05$ ).

**Table 1:** Chemical composition of Sr-doped forsterite powders.

Sample name	Composition ( wt.%)				Sr (wt.%)	Mg /Si (mol ratio)	Sample composition
	Mg(NO <sub>3</sub> ) <sub>2</sub> ·6H <sub>2</sub> O	Sr(NO <sub>3</sub> ) <sub>2</sub>	C <sub>12</sub> H <sub>22</sub> O <sub>11</sub>	PVA			
F0	15.59	-	83.08	1.34	0	2	Mg <sub>2</sub> SiO <sub>4</sub>
F1	15.17	0.32	83.16	1.34	3.05	1.95	Mg <sub>1.95</sub> Sr <sub>0.05</sub> SiO <sub>4</sub>
F2	14.84	0.64	83.18	1.34	5.96	1.9	Mg <sub>1.9</sub> Sr <sub>0.1</sub> SiO <sub>4</sub>
F3	14.08	1.29	83.29	1.34	11.43	1.8	Mg <sub>1.8</sub> Sr <sub>0.2</sub> SiO <sub>4</sub>
F4	12.54	2.58	83.53	1.34	21.11	1.6	Mg <sub>1.6</sub> Sr <sub>0.4</sub> SiO <sub>4</sub>

**Table 2:** The detailed crystal structure analysis of the as-synthesized Sr-forsterite powders.

Sample	Phase composition ( wt.%)				Crystallite size (nm)	Particle size (nm)	a(°Å)	b(°Å)	c(°Å)
	Mg <sub>2</sub> SiO <sub>4</sub>	MgO	Sr <sub>2</sub> MgSi <sub>2</sub> O <sub>7</sub>	MgSiO <sub>3</sub>					
F0	100	0	0	0	25.3	31.0 ± 3.9	4.755	10.210	5.986
F1	92.65	0	0	7.35	27.7	40.7 ± 6.1	4.757	10.214	5.988
F2	69.78	22.60	3.54	4.08	43.9	45.9 ± 5.9	4.758	10.216	5.989
F3	70.15	9.41	20.44	-	45.8	62.9 ± 11.8	4.760	10.220	5.994
F4	60.44	-	39.56	-	25.3	-	4.753	10.204	5.986